Nanoscale

Accepted Manuscript

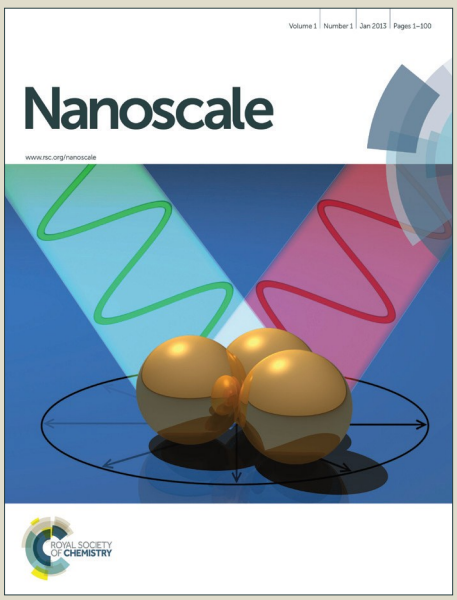

ROYAL SOCIETY OF CHEMISTRY

www.rsc.org/nanoscale

Journal Name

ARTICLE

Morphology Evolution of Single-Crystalline Hematite Nanocrystals: Magnetically Recoverable Nanocatalyst for Enhanced Facets-Driven Photoredox Activity

Received 00th January 20xx,
Accepted 00th January 20xx

DOI: 10.1039/x0xx00000x

www.rsc.org/

Astam K. Patra,[a] Sudipta K. Kundu,[b] Asim Bhaumik,[b] Dukjoon Kim[a]*

We have developed a new green chemical approach for the shape-controlled synthesis of single-crystalline hematite nanocrystals in aqueous medium. FESEM, HRTEM and SAED techniques were used to determine morphology and crystallographic orientations of each nanocrystal and its exposed facets. PXRD and HRTEM techniques revealed that the nanocrystals are single crystalline in nature; twins and stacking faults were not detected in these nanocrystals. The structural, vibrational, and electronic spectra of these nanocrystals were highly dependent on their shape. Different shaped hematite nanocrystals with distinct crystallographic planes have been synthesized in similar reaction conditions, which can be desired as a model for the purpose of properties comparison than the nanocrystal prepared under different reaction condition. Here we investigated the photocatalytic performance of these shaped-nanocrstyals for methyl orange degradation in the presence of white light (λ>420 nm). In this study, we found that the density of surface Fe^{3+} ions in a particular facets was the key factor for the photocatalytic activity and was higher on the bitruncated-dodecahedron shaped nanocrystals by coexposed {104}, {100} and {001} facets, attributing to higher catalytic activity. The catalytic activity of different exposed facets nanocrystals were as follows: {104}+{100}+{001} (bitruncated-dodecahedron) >{101}+{010} (bitruncated-octahedron) >{001}+{110} (nanorods) >{012} (nanocuboid) which provided the direct evidence of exposed facets-driven photocatalytic activity. The nanocrystals were easily recoverable using external magnet and reused at least six times without significant loss of its catalytic activity.

Introduction

Crystal growth engineering has attracted the attention of many researchers conducting studies in solid-state materials chemistry. Crystalline nanocrystals, having a particular shape and exposed facets, possess excellent physical and chemical properties; this is attributed to the different electronic and atomic arrangements in the exposed facets.[1-4] The shape of nanocrystals depends on the crystallographic structure of a particle surface, which also governs its distinct properties, such as reactivity, selectivity, adsorption capacity, electrical conductivity, and optical properties.[5-7] Several researchers have made intensive efforts to design and control the morphological architecture of nanocrystals, because they exhibit a unique size- and shape-dependent phenomena. However, using a chemical method, it is quite difficult to adjust the particular shape of nanocrystals.[8,9] In most advanced studies of crystal growth engineering, researchers have tried to vary the surface crystallographic orientation of Ag, Au, Pd, and Pt-based noble-metal nanostructures.[10-17] On the other hand, it is even more difficult and challenging to carry out surface engineering of metal-oxides.[18] Among different metal oxides, hematite (α-Fe_2O_3) is thermodynamically very stable under ambient conditions. Hematite has received extensive attention of researchers as it can be used in diverse applications, including catalysis,[19,20] magnetic devices,[21,22] environmental protection,[23] gas sensors,[24] drug delivery,[25] pigments and paints, Li ion battery,[26,27] water splitting[28,29] etc. It has low band gap energy (E_g = 2.2 eV). Moreover, it is a cheap metal oxide that is non-toxic and environmentally friendly. Furthermore, it also has relatively good stability and magnetically recoverable. Owing these attractive features, hematite is widely used in diverse applications.[30-32] In the past decades, researchers have developed many synthetic strategies, such as the hydrothermal process, sol-gel process, and thermal decomposition methods that could be used to prepare 1D, 2D and 3D hematite materials.[30, 33-36] Recent studies have reported that hematite particles, having the shape of polyhedron, possess outstanding properties as they have different high-index exposed facets. In 2010, Sun and co-workers[37] synthesized dodecahedral shape nanocrystal which was enclosed by twelve (101) crystal planes, and octodecahedral shape nanocrystal enclosed by twelve (101) and six (111) planes. Compared to the hematite particles reported in previous studies, these dodecahedral and octodecahedral particles had a much stronger magnetic character.

[a] School of Chemical Engineering, Sungkyunkwan University, Suwon, Kyunggi, 440-746 (Republic of Korea), E-mail: djkim@skku.edu
[b] Department of Materials Science, Indian Association for the Cultivation of Science, 2A & B, Raja S.C. Mullick Road, Jadavpur, Kolkata-700032 (India), E-mail: msab@iacs.res.in
Electronic Supplementary Information (ESI) available: See
DOI: 10.1039/x0xx00000x

They also possessed different magnetic properties. Yin *et al.*[33] have also reported about the peculiar magnetic properties of tetrakaidecahedral and oblique parallelepiped hematite nanocrystals with exposed high index facets. Liu *et al.*[37] reported quasi-cubic hematite nanocrystals enclosed by (012), (10-2) and (1-12) facets and hexagonal bipyramidal hematite nanocrystals enclosed by (012) facets show shape- and surface-dependent magnetic properties. In 2012, Zhou *et al.*[38] carried out visible-light-induced RhB degradation on hematite particles: the process was strongly dependent on the architecture of nanocrystals, while the order of reactivity of the exposed facets followed the sequence: {001}{110} faceted nanorod > {012} faceted nanocube > {001} faceted nanoplate. Zhao *et al.*[39] have reported that rhombohedral hematite crystals have {0001} and {10-10} exposed facets, but truncated dodecahedron-crystals are predominantly characterized by {10-12} exposed facets. The photocatalytic performance of truncated dodecahedron crystals was superior to that of rhombohedral crystals. This discrepancy in photocatalytic behaviour of crystals is because the surface density of Fe ions on particular facets. Recently, Ouyang *et al.*[40] have synthesized the following kinds of nanocrystals: hexagonal bipyramids with {113} facets, pseudocubes with {012} facets, and nanoplates with {001} facets. In these nanocrystals, the ease of catalytic oxidation with CO followed the following sequence of facets: {012} > {113} > {001}. The bipyramidal hematite-{113} nanocrystals exhibited the best performance in acetone sensing, followed by pseudocubic hematite-{012} and plate hematite-{001}/{012}. The same facet-dependent sensing order {113} > {012} > {001} was found while analysing the three samples with methanol sensing. So there has been recent increasing interest in the preparation of polyhedral hematite single crystals with exposed different facets to find exceptional properties. Recently Lin *et al.*[41] have synthesized hexagonal bipyramidal hematite nanocrystals by adding F^- anions and they reported that there are two surfaces that are most stable facets in the hematite crystals: {113} facets that are easily adsorbed with F^- ions, and the {104} facets that are stabilized by OH^-. It is still a challenge to synthesize different shaped single crystalline hematite with environmentally friendly process in similar reaction conditions. In this context, we have synthesized different shaped hematite nanocrystals, with low energy exposed facets {001} and high energy exposed facets {101} in same chemical synthesis method. It is noted that the morphology of crystals and exposed facets is governed by temperature. We have synthesized nanocrystals of different morphologies by simply tuning the reaction temperature. This is because the growth of nanocrystals is related to the surface energy of the growth plane. We successfully synthesized nanocrystals with the different shape and exposed facets: {001}, {110}, {012}, {100}, {104} and {101}. The nanocrystals exhibit high photocatalytic activity when subjected to dye degradation in the presence of white light. A significant portion of dyes gets wasted in the dying processes, and the effluents are released into water streams. Dye molecules are hazardous as they cause various health problems and serious environmental problems all over the world. So, researchers are of the view that dye molecules must be mineralized in aqueous solutions using sunlight with the photocatalyst.

Scheme 1. Synthetic Route of Shaped-Nanocrystals via Hydrothermal Synthesis Method.

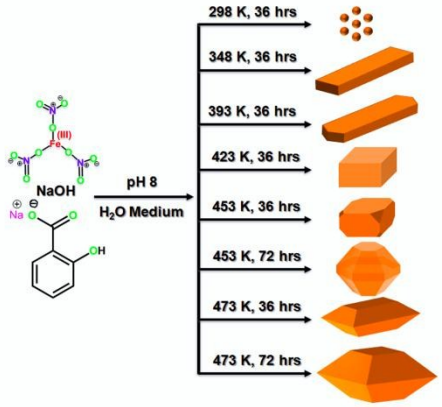

Experimental Section

Materials: All the chemicals used in this study were of ACS grade [illegible] they were not subjected to further purification. Sodium salicylate (SS, Sigma Aldrich 99%), ferric nitrate nonahydrate ($Fe(NO_3)_3{\cdot}9H_2O$, Sigma Aldrich 98%), sodium hydroxide (NaOH, Sigma Aldrich 97%) were purchased from Sigma Aldrich In this study, we carried out [illegible] the chemical reactions in deionised water.

Synthesis procedure of Nanocrystals with different Morphologies

We synthesized nanocrystals of different shapes using the hydrothermal synthesis method. This experimental method of synthesis was carried out at different temperatures, and the duration of the process was varied accordingly. However, the remaining factors were constant while synthesizing different nanocrystals. In this synthesis process, 10 mmol of sodium salicylate and 12.5 mmol of NaOH were mixed with 20 mL of water. Then, 1 mmol of $Fe(NO_3)_3{\cdot}9H_2O$ was dissolved in 5.0 g of water, and this solution was slowly added to the reaction solution. We added 2M NaOH solution slowly to the reaction solution till its pH was adjusted to 8. The resultant mixture was stirred for 3 hrs. Then, this reaction mixture was transferred into a Teflon-lined stainless steel autoclave and hydrothermally treated at requisite temperature for a fixed duration of time. Scheme 1 and Table S1 provides a detailed summary of the synthesized material, hydrothermal temperature and time required for the completion of synthesis. The resultant dark red coloured solid was separated by centrifugation. Then, this solid was washed several times with water and ethanol. The synthesized material was dried at room temperature under vacuum. Furthermore, the material was extracted with acid-ethanol solution to remove the salicylate moiety from the material. The FTIR analysis (Fig. S1) was confirmed that salicyaltes were removed from the materials. This material was used in photocatalysis.

Photocatalytic Test

The photocatalytic activity of hematite nanocrystals was determined by performing the degradation of methyl orange dye in the presence of white light (λ>420 nm). 1000 ml of 0.02 mM solution was prepared. Prior to measurement, 50 mL of 0.02 mM solution was mixed with 10 mg of hematite nanocrystals in a round bottle flask of 100 ml capacity. Before photo-irradiation, the

catalyst was added to the reactant solution and then it was stirred vigorously for 30 min in the dark. Thus, we established the adsorption–desorption equilibrium. Then, 0.5 mL of H_2O_2 (30 % wt) solution was added as an additive to the reactant solution. The reactant solution was irradiated with white light using a solar simulator of 150 W power xenon lamp (Newport Corporation) with 420 nm cut off filter and stirred magnetically to maintain the homogeneity of the suspension. However, at regular intervals of time (20 min), 1 mL of the reactant solution was withdrawn and centrifuged to remove the catalyst from the suspension. After the completion of the reaction, the magnetic catalyst was recovered by an external magnet and the solution was decanted. The nanocatalyst was washed thoroughly with water and ethanol. The dye concentration in the solution phase was calculated from the absorbance values, which were measured using the UV 2401PC UV-visible spectrophotometer. The intermediates products of methyl orange degradation were identified by liquid chromatograph-mass spectrometer (Agilent Model 1100 LCMS ion trap with C18 Column and negative ion mode, ESI). 10 μL of aliquot was injected for analysis and acetonitrile-water mixture (30:70) was used as eluent with column temperature 298 K and 1 mL/min flow rate.

Recyclability of the photocatalyst

We examined whether hematite could be reused as a nanocatalyst in the reaction involving the degradation of methyl orange dye by white light. After the completion of the reaction, the magnetic catalyst was recovered by an external magnet and the solution was decanted. The nanocatalyst was washed thoroughly with water and ethanol. For activating this catalyst for the next reaction, it was dried at 348 K for 4 hrs under vacuum. Thus, this nanocatalyst was recycled and used in subsequent experiments. The recycling reactions were performed six times under identical conditions.

Characterization

The size, shape, morphology, band gap, and structural features of goethite and hematite nanocrystals are investigated using different characterization techniques. Powder X-ray diffraction patterns of the samples were recorded on a Bruker D-8 Advance diffractometer; this instrument was operated at voltage of 40 kV and current of 40 mA using Cu Kα (λ = 0.15406 nm) radiation. Raman spectroscopy measurements were recorded using a Bruker Senterra Raman microscope. In this process, the samples were excited at room temperature by subjecting them to a laser beam of 532 nm; the samples were exposed to this excitation laser beam for 30 s at 1 mW power. TEM images and HRTEM and SAED patterns were recorded with a JEOL JEM-2100F TEM that was operated at 200 kV. A JEOL JEM- 7600F field-emission scanning electron microscope (FE SEM) was used for conducting morphology analysis. Nitrogen sorption isotherms were obtained at 77 K using an ASAP 2000 surface area analyzer (Micromeritics Instrument Corporation, Georgia, USA). Prior to the measurement, the samples were degassed at 423K for 3 hrs. UV-visible diffuse reflectance spectra were recorded on a UV 2401PC UV-visible spectrophotometer (Shimadzu Corporation, Kyoto, Japan) using an integrated sphere attachment. $BaSO_4$ was used as the background standard in the spectrophotometric analysis. The photocatalysis was conducted by illuminating with white light produced from a solar simulator of

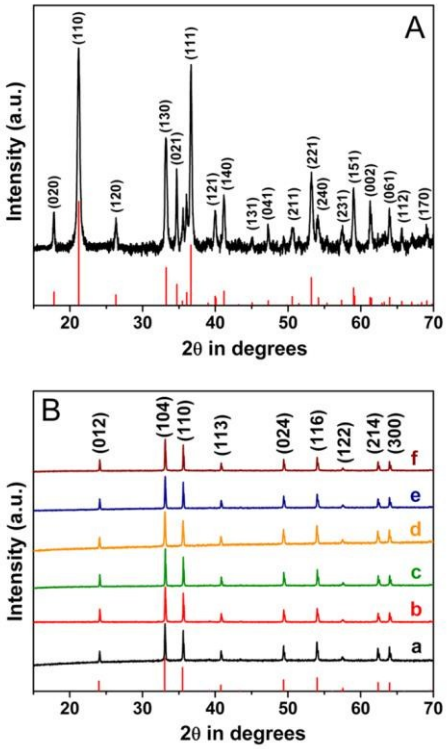

Fig. 1. A) Wide-angle XRD pattern of the goethite nanorods (S75-NR). All the peaks are indexed to goethite phase (α-FeOOH). B) Wide-angle XRD pattern of the highly crystalline hematite nanocrystals. a) nanorods b) nanocuboids, c) irregular shaped nanocrystals, d) bitruncated-dodecahedron, e) bitruncated-elongated octahedron and f) bitruncated-octahedron nanocrystals. All the peaks are indexed to hematite phase (α-Fe_2O_3).

150-W power xenon lamp (one Sun) (Newport Corp., USA; Model 69907). The intermediates of methyl orange degradation were monitored by liquid chromatograph-mass spectrometer (Agilent Model 1100).

Result and discussion

Structural and vibrational information from PXRD and Raman analysis

Powder X-ray diffraction (PXRD) analysis was used to determine the structural features, crystallinity, and purity of nanocrystals synthesized in this study. The nanocrystals were synthesized by hydrothermal synthesis method. This method was performed at different temperatures using iron nitrate nonahydrate as the precursor. Sodium salicylate was used as the capping agent, while sodium hydroxide was used as the bridging ligand and deionised water was used as the solvent. The reaction procedure had to be carried out for different durations to synthesize different nanocrystals. The reaction details are shown in scheme 1 and table S1. Fig. S2 shows that the nanocrystals (S25-NP) were synthesized at 298 K by performing the reaction for 36 hrs. S25-NP nanocrystals were semi-crystalline in nature. S75-NR nanocrystals were synthesized at 348 K by carrying out the reaction for 36 hrs. S75-NR nanocrystals are highly crystalline in nature (Fig. 1A).

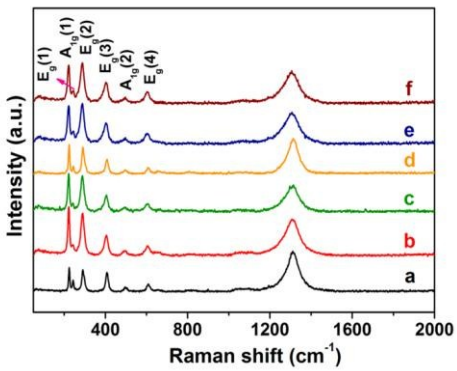

Fig. 2. Raman spectra of different-shaped hematite nanocrystals. (a) nanorods, (b) nanocuboids, (c) irregular shape nanocrystals, (d) bitruncated-dodecahedron, (e) bitruncated-elongated octahedron, (f) bitruncated-octahedron nanocrystals.

This indicates that crystal growth was favoured at high temperature, and highly crystalline nanocrystals were obtained at higher temperatures. The 2θ diffraction positions of these nanocrystals (S25-NP and S75-NR) corresponded with the goethite (α-FeOOH) phase (JCPDS PDF number 01-081-0463)[42,43] in both the samples. All the peaks matched with a pure orthorhombic crystal system having a Pbnm space group and lattice parameters: a = 0.461, b = 0.995 and c = 0.302 nm. When the hydrothermal temperature was increased beyond 423 K, we obtained highly crystalline nanocrystals (Fig. 1B), and the 2θ diffraction positions matched with the hematite (α-Fe_2O_3) phase (JCPDS PDF number 01-084-0308).[33,44] All the peaks corresponded with a rhombohedral crystal system, having an R-3c space group and lattice parameters: a = 0.501 and c = 1.367 nm. These PXRD analyses indicate that iron hydroxide nanocrystals are produced at low temperature. At higher temperatures, the iron hydroxides get transformed into iron oxides. No peaks of impurity were observed in this experimental study, because we obtained single crystalline materials of high purity. In hematite nanocrystals, the relative peak intensity of different growth planes increased with an increase in the temperature and reaction duration of hematite syntheses. The details of the relative peak intensity are given in Table S2. From the analysis, we found that the relative peak intensity of the (110) planes is higher for hematite nanocrystals which have the shape of nanorods. The relative peak intensity of the (110) planes increases as the $I_{(012)}/I_{(110)}$ and $I_{(104)}/I_{(110)}$ ratio decreases. In nanocrystals of nanocuboid shape, the relative peak intensity of (012) planes increase with an increase in $I_{(012)}/I_{(104)}$ ratio. In the bitruncated dodecahedron nanocrystals, the relative peak intensity of (104) planes was found to increase with an increase in $I_{(104)}/I_{(110)}$ ratio and a decrease in $I_{(012)}/I_{(104)}$ ratio. The relative peak intensity of (012) and (110) planes was found to increase in bitruncated-elongated octahedron and bitruncated Octahedron nanocrystals.

Furthermore, Raman spectroscopy measurements were carried to determine how the chemical environment of different morphologies changed in the presence of light. It is a well-known fact that different facets of nanocrystals have different chemical environments, which immensely influence the properties of nanocrystals.[45] Fig. 2 displays the Raman spectra of different hematite nanocrystals having different shapes. The frequencies of Raman bands observed at 222.3, 244.0, 288.9, 405.5, 497.0, and 662.0 cm^{-1} were assigned to $A_{1g}(1)$, $E_g(1)$, $E_g(2)$, $E_g(3)$, $A_{1g}(2)$, and $E_g(4)$ vibration modes, respectively.[46] One broad peak that appeared at 1310 cm^{-1} was attributed to a two-magnon scattering mode.[47,48] In particular, all the observed Raman peaks were attributed to hematite. No other peaks were detected in the Raman spectra, indicating that this simple method could only synthesize hematite. Moreover, the synthesized hematite did not contain impurities, such as iron hydroxides, iron oxides and/or oxyhydroxides. Interestingly, the relative intensity between E_g and A_{1g} peaks was found to be different for different shapes of nanocrystals (see Table S3). The E_g and A_{1g} ratio was highest for the nanorod, but lowest for nanocuboids. Thus, the Raman spectroscopy measurements confirm the XRD results, indicating that the nanocrystals were of pure hematite. The corresponding changes in relative intensity peaks were attributed to the different morphologies of these nanocrystals.

Surface morphology analysis by FE SEM

Fig. 3 displays the high resolution field-emission scanning electron microscope (FE-SEM) images, and the schematic drawings of the corresponding goethite and hematite nanocrystals. We found that the surface morphology and the size of goethite and hematite nanocrystals were uniform throughout the product for a particular reaction. Furthermore, the size of nanocrystals increased and the shape also changed when we increased the hydrothermal temperature and the duration of these syntheses reactions. We found that variation in synthesis temperature brought about morphological changes in the nanocrystals. The nanocrystals synthesized by this method had sharp edges. Moreover, we could clearly see the faces of all the nanocrystals. Fig. 3a displayed the small-sized goethite nanoparticles, which were obtained at room temperature by carrying out the hydrolysis of iron nitrate. Furthermore, by increasing the synthesis temperature, we obtained goethite nanorods with 6 faces, 8 vertices, and 12 edges (Fig. 3b). The average length, width, and height of these nanorods are *ca* 150, 25, and 12 nm, respectively. By performing hydrothermal synthesis at 393K, we obtained hematite nanorods with 8 faces, 12 vertices, and 18 edges (Fig. 3c). By performing hydrothermal synthesis at 423 K, we obtained nanocuboids with 6 faces, 8 vertices, and 12 edges (Fig. 3d). Fig. 3e shows an FE-SEM image of hematite nanocrystals having an irregular shape. The size of these nanocrystals was in the range 200-300 nm diagonally; these irregular shaped nanocrystals were obtained at 453 K by performing the hydrothermal reaction for 36 hrs. But, when we carried out the hydrothermal synthesis for 72 hrs at the same reaction temperature, nanocrystals of bitruncated dodecahedron (Fig. 3f) shape were obtained; they had 20 faces, 24 vertices, and 42 edges. Fig. 3g and 3h illustrates that nanocrystals, having the shape of bitruncated-elongated octahedron and bitruncated-octahedron, had 10 faces, 12 vertices, and 20 edges; these types of nanocrystals were obtained by carrying out the hydrothermal temperature at 473 K; the size difference was attributed to increasing the duration of the hydrothermal reaction from 36 hrs to 72 hrs. In this study, all the three-dimensional nanocrystals comply with Euler's Formula, which links the numbers the vertices (V), faces (F), and edges (E)

Table 1. Physical and chemical properties of hematite (α-Fe_2O_3) nanocrystals obtained under different condition of syntheses. % of dominant exposed facets are also reported.

Sample	Morphology	Length (nm)	Width (nm)	Height (nm)	No of face (F), vertex (V) and edge (E)	% of Dominant facets
S120-NR	Nanorod	430±50	33±2.4	16±1.3	F-8, V-12, E-18	74.2%{001}+25.8%{110}
S150-NC	Nanocuboid	240±35	205±35	95±10	F-6, V-8, E-12	100%{012}
S180-BTD	Bitruncated-dodecahedron	325±50	240±25	220±10	F-20, V-24, E-42	27%{001}+50.4%{104}+22.6%{100}
S200-BTEO	Bitruncated-elongated octahedron	300±50	150±35	150±30	F-10, V-12, E-20	3.5%{001}+96.5%{101}
S200-BTO	Bitruncated-octahedron	340±50	250±20	160±10	F-10, V-12, E-20	5.2%{001}+94.8%{101}

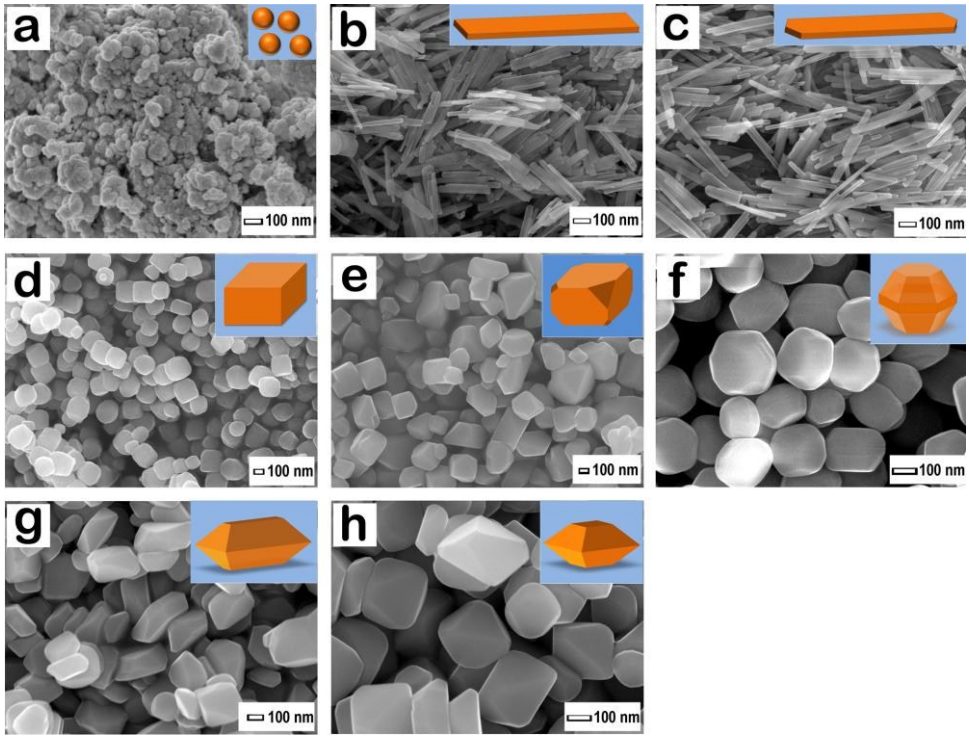

Fig. 3. High resolution FE-SEM images of goethite and hematite nanocrystals. (a) goethite nanoparticles, (b) goethite nanorods, (c) hematite nanorods, (d) hematite nanocuboids, (e) hematite irregular-shaped nanocrystals, (f) hematite bitruncated-dodecahedron, (g) hematite bitruncated-elongated octahedron, (h) hematite bitruncated-octahedron.

of a polyhedron as V+F–E=2. Therefore, the synthesized nanocrystals with definite shape are geometrically stable. Table 2 summarizes the length, width, height, and number of faces, vertices, edges, and % of dominant facets of hematite nanocrystals.

Nanostructure and exposed facets analysis by HR TEM

High resolution transmission electron microcopy (HR TEM) was used to investigate the shape, size, crystal growth direction, and different surfaces of exposed facets of the nanocrystals. Fig. S3 shows the TEM image of goethite nanoparticles synthesized at room temperature. We found that through the specimen, the particles had a uniform size of 4-5 nm. The different morphologies of nanocrystals, which were obtained by the hydrothermal synthesis method, were examined using high-resolution transmission electron microscopy (HRTEM) and selected area electron diffraction (SAED) techniques.

Goethite Nanorod

Fig. 4a shows the TEM image of goethite nanocrystals synthesized at 348 K for 36 hrs. These nanocrystals have the shape of a nanorod. Nanorods of uniform size are seen throughout the specimen. Furthermore, different crystalline planes of individual nanorods are also clearly seen in Fig. 4b. A closer view of the image in Fig. 4b is taken from the left hand side, and different classes of lattice fringes are resolved in Fig. 4c. The lattice spacing in the nanorod is 0.418 and 0.298 nm, corresponding to the (110) and (001) lattice planes

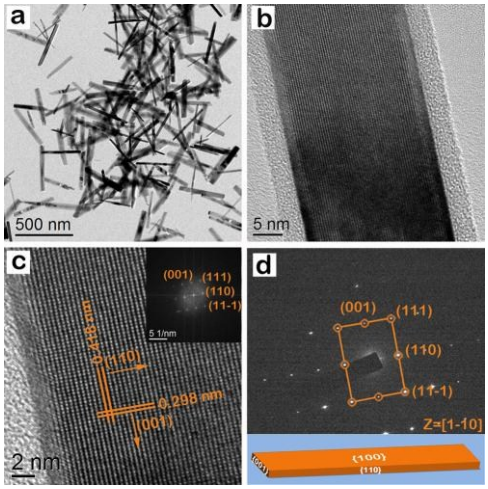

Fig. 4. a) TEM image of goethite nanocrystals having the shape of nanorods. b) HRTEM image of a single nanorod. c) HRTEM image of a single nanorod having a lattice plane with (110) and (001) indices, and the corresponding FFT pattern indexing (001), (111), (110), and (11-1) lattice spots. d) SAED pattern of the nanorod having lattice spots with (001), (111), (110) and (11-1) indices. The measured angle between (001) and (110) lattice planes is 90°. Fig. 4d shows the geometrical model of a goethite nanocrystal with exposed facets; this nanocrystal has the shape of a nanorod.

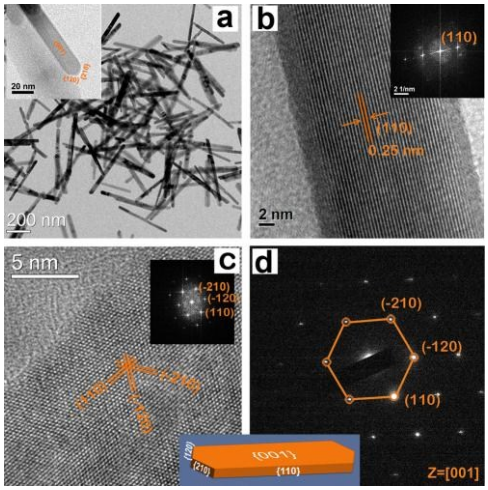

Fig. 5. a) TEM image of hematite nanocrystals, having the shape of nanorods b) HRTEM image of a single nanorod, having a lattice plane with (110) indices; the corresponding FFT pattern had a lattice spot with (110) indices. c) A highly magnified HRTEM image of a single nanorod, having lattice planes with (110), (-120), and (-210) indices; the corresponding FFT pattern has lattice spots with (110), (-120), and (-210) indices, d) SAED pattern of the nanorod, having lattice spot with (110), (-120), and (-210) indices. The measured angle between (102) and (-120) lattice planes is 60°. Inset of Fig. 5 shows a geometrical model of hematite nanocrystals with exposed facets; these nanocrystals have the shape of nanorods.

goethite crystal phase, respectively. The interfacial angle between (110) and (001) lattice planes is 90°, while the corresponding FFT pattern (inset of Fig. 4c) is composed of (001), (111), (110), and (11-1) lattice spots. As shown in Fig. 4d, the selected-area electron diffraction (SAED) pattern displayed (001), (111), (110), and (11-1) lattice spot along the [1-10] zone axis[50]. This indicates that the nanocrystals have well-defined diffraction spots for the goethite crystals. The analysis shows that the top surface of the particle has {100} facet. After analyzing HRTEM and SAED images, we infer that goethite nanocrystals are single crystalline in nature. They have the shape of nanorods and are enclosed by two {100}, two {110}, and two {001} exposed facets. So, the enclosing lattice planes are (100), (-100), (110), (1-10), (001), and (00-1). Fig. 4d is a representative geometrical model of the goethite nanocrystals, having the shape of nanorods.

Hematite Nanorod

Fig. 5a shows the TEM image of hematite nanocrystals, having the shape of nanorods. These nanocrystals were synthesized at 393 K for 36 hrs. Nanorods of uniform size are seen throughout the specimen. Fig. 5a displays an individual nanorod head that clarifies its exposed facets. Fig. 5b clearly displays an individual nanorod with (110) lattice fringes; the corresponding FFT pattern is shown in the inset of this Fig. 5b. Fig. 5c shows a highly magnified image of the individual nanorod, and the three classes of lattice fringes are resolved. The lattice spacing of the nanorod is 0.25 nm, which corresponds to (110) and its equivalent lattice planes in a hematite crystal. The interfacial angle between them is found to be 60°, and the corresponding FFT pattern (inset of Fig. 5c) is associated with (110), (-120), and (-210) lattice spots. Fig. 5d shows the SAED pattern displaying (110), (-120), and (-210) lattice spots along the [001] zone axis.[51] This indicates that the nanocrystals have

well-defined diffraction spots in hematite crystals. Based on our analysis, we infer that the top surface of the particle is {001} facet. Based on the analysis of HRTEM and SAED images, we infer that hematite nanocrystals are single crystalline in nature; these nanocrystals have the shape of nanorods and are enclosed by two {001}, two {110}, two {120} and two {210} exposed facets. So, the enclosing planes are (001), (00-1), (110), (-1-10), (-120), (1-20), (-210), and (2-10) in the hematite nanocrystal. Fig. 5 is a representative geometrical model of the hematite nanocrystals with exposed facets; these nanocrystals have the shape of nanorods.

Hematite Nanocuboid

Fig. 6a shows the TEM image of hematite nanocrystals, having the shape of nanocuboids. These nanocrystals were synthesized at 423 K for 36 hrs. nancuboids of uniform size are seen throughout the specimen. HRTEM images are shown in Fig. 6b. The lattice spacing is 0.36 nm in both the cases, corresponding with the (012) and its equivalent lattice planes in hematite crystals. The interfacial angle between (012) and (-102) plane is 94°. Fig. 6c shows SAED pattern which is taken in the region marked 'c' of Fig. 6a. The diffraction spots are attributed to (110), (012), (1-1-4) and (-102) lattice spots along the [2-21] zone axis.[52] The analysis shows that the top surface of the particle is {112} facet. The sharp diffraction spots in SAED pattern reveal the single crystalline nature of the hematite nanocrystals, having the shape of nanocuboids. These nanocrystals are enclosed by two {012}, two {102}, and two {112} exposed facets. So, the enclosing planes are (012), (0-1-2), (-102), (10-2), (1-12), and (-11-2). Fig. 6d shows a representative geometrical model of the hematite nanocrystal with exposed facets; these nanocrystals are nanocuboid in shape.

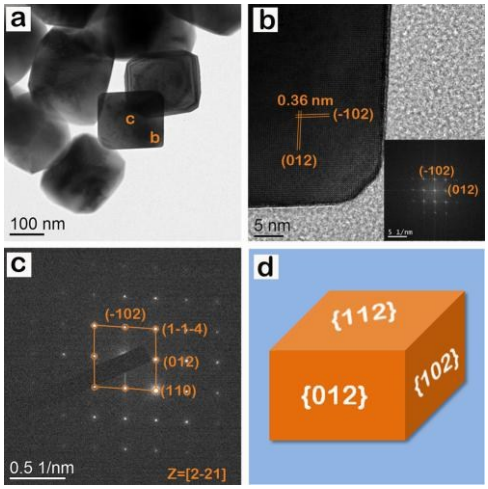

Fig. 6. a) TEM image of hematite nanocrystal, having the shape of nanocuboids b) HRTEM image and the corresponding FFT pattern (inset) have lattice spots with (-102) and (012) indices. c) SAED pattern with lattice spots having (110), (012), (1-1-4) and (-102) indices. The measured angle between (-102) and (012) is 94°. d) Geometrical model of hematite nanocrystal with exposed facets; these nanocrystals are nanocuboid in shape.

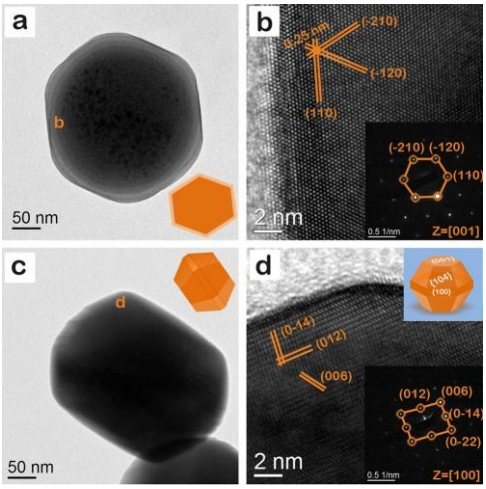

Fig. 7. a) TEM image of bitruncated hematite nanocrystals, having the shape of a dodecahedron. The TEM image is a geometrical model of these nanocrystals (top view). b) HRTEM image and corresponding SAED pattern (inset), which is area marked 'b' in Fig. 7a. The SAED pattern displays lattice spots with (110), (-120), and (-210) indices. The measured angle between them is 60°. c) The geometrical model (side view) of TEM image of the nanocrystal in another orientation. d) HRTEM image and the corresponding SAED pattern (inset) in area marked 'd' in Fig. 7c; this SAED pattern has lattice spots with (012), (006), (0-14), and (0-22) indices. The measured angle between (012) and (0-14) is 85°. The inset of Fig. 7d shows the geometrical model of the bitruncated hematite nanocrystal with exposed facets; these nanocrystals have the shape of a dodecahedron.

Hematite Bitruncated-Dodecahedron

Fig. 7a shows the representative TEM image of hematite nanocrystals and its geometrical model (inset of Fig. 7a). These nanocrystals have the shape of a bitruncated dodecahedron. Fig. 7b and its inset show the HR TEM image and the corresponding SAED pattern, which is taken in the region marked as b in Fig. 7a. In Fig. 7b, the lattice spacing is 0.25 nm, which corresponds with (110) and its equivalent lattice planes in a hematite crystal. The interfacial angle between them is 60°. In the SAED pattern, the diffraction spot is attributed to (110), (-120), and (-210) lattice spots along the [001] zone axis.[51] The analysis suggests that the top surface of the particle is {001} facet. Fig. 7c shows another orientation of the hematite nanocrystals and its geometrical model (inset of Fig. 7c). These nanocrystals have the shape of a bitruncated-dodecahedron. Fig. 7d and its inset show the HR TEM image and the corresponding SAED pattern, which is taken in the region marked d in Fig. 7c. The lattice spacing is 0.36, 0.27, and 0.23 nm, corresponding with the (012), (0-14), and (006) lattice planes in a hematite crystal. The interfacial angle between (012) and (0-14) is 85°. In the SAED pattern, the diffraction spot is attributed to (012), (006), (0-14), and (0-22) lattice spots along the [100] zone axis.[40,53] The analysis suggests that the side surface of the particle is {104} facet. The sharp diffraction spots in both SAED patterns reveal the single crystalline nature of hematite nanocrystals, having the shape of a bitruncated-dodecahedron. These nanocrystals are enclosed by two {001}, twelve {104}, and six {100} exposed facets. So, the enclosing planes are (001), (00-1), (104), (0-14), (-114), (10-4), (01-4), (-1-14), (-104), (0-14), (-11-4), (-10-4), (0-1-4), (11-4), (100), (-100), (1-10), (-110), (0-10), and (010). The inset of Fig. 7d shows a representative geometrical model of the hematite nanocrystal with exposed facets; these nanocrystals have the shape of a bitruncated-dodecahedron

Hematite Bitruncated-Octahedron

Fig. 8 and Fig. S4 display the representative TEM image of different hematite nanocrystals, having the shape of an octahedron. Fig. 8b and its inset show the HR TEM image and the corresponding SAED pattern, which is taken in the region marked 'b' in Fig. 8a. In Fig. 8b, four sets of lattice fringes are clearly observed. The lattice spacing is 0.41, 0.41, 0.36, and 0.25 nm, corresponding with the (101), (0-11), (1-12), and (110) lattice planes of hematite crystals. In the SAED pattern, the diffraction spot is attributed to (110), (101), (1-12), and (0-11) lattice spot along the [1-1-1] zone axis.[36] The analysis shows that the mark surface 'b' of the particle is {101} facet. Fig. 8c shows HR TEM image and the corresponding SAED pattern of another surface of the nanocrystals, having the shape of a bitruncated octahedron. HRTEM image and the corresponding SAED pattern analysis showed that the surface is equivalent to {101} facet. The sharp diffraction spots in both SAED patterns revealed the single crystalline nature of the nanocrystals, having the shape of a bitruncated octahedron. These nanocrystals are enclosed by two {001} and eight {101} exposed facets. So, the enclosing lattice planes are (001), (00-1), (101), (011), (-101), (0-11), (10-1), (01-1), (0-1-1), and (-10-1). Fig. 8d shows a representative geometrical model of a hematite nanocrystal with exposed facets; this nanocrystal has the shape of bitruncated octahedron.

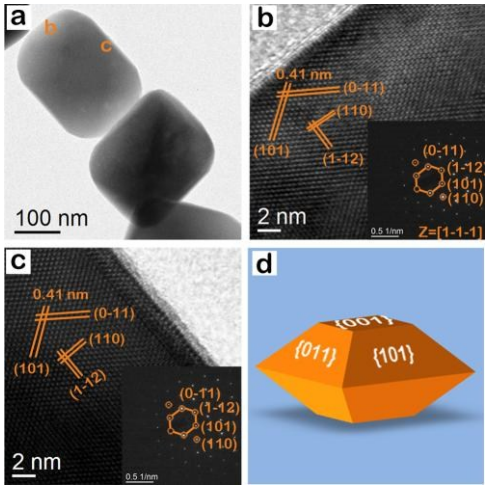

Fig. 8. a) TEM image of hematite nanocrystal, having the shape of a bitruncated-octahedron. b) HRTEM image and the corresponding SAED pattern (inset), which is taken from the area marked 'b' in Fig. 8a; this SAED pattern shows lattice spots with (110), (101) (1-12) and (0-11) indices. c) HRTEM image and the corresponding SAED pattern (inset), which is taken from the area marked 'c' in Fig. 8a; this SAED pattern shows lattice spots with (110), (101), (1-12), and (0-11) indices. The angle between (101) and (0-11) lattice spots is 110°, while the angle between (101) and (1-12) is 55° in both diffraction patterns. d) Geometrical model of a hematite nanocrystal with exposed facets; this nanocrystal has the shape of a bitruncated octahderal.

Growth Mechanism of Single-Crystals

We could understand how temperature affected the growth of crystals in this syntheses method. In this study, we varied only the temperature and duration of reaction for synthesizing nanocrystals of different shapes. But, other parameters, such as template and Fe^{3+} concentration, pH, volume of the reaction mixture, solution medium, etc were kept constant. The growth of crystals is a complicated process, which is highly dependent on the surface energy and atomic arrangements of the crystal's facets. Different facets grow at different rates during the growth of a crystal. Typically, low-energy facets have slower growth rates than high-energy facets. Overall, the final crystal shape is governed by the slow-growing facets and the shapes of energy minima.[4,8] A crystal's growth is also highly related to temperature, since the Gibb's free energy of formation depends on the temperature of the critical nucleus.[54] In this study, we obtained nanocrystals with different crystal facets by tuning the reaction temperature (SEM and TEM analysis). In these syntheses, iron nitrate nonahydrate was used as a precursor, and sodium salicylate was used as the capping agent. Furthermore, sodium hydroxide was used as the bridging ligand, while water was used as the solvent. Sodium salicylate is widely used to control the morphology and nanostructure of metal oxides.[55-57] The hydroxide anion (bridging agent) facilitates the formation of Fe-O-Fe skeleton,while the salicylate moiety of the capping agent inhibits the formation of Fe-O-Fe skeleton. This is because there is a covalent interaction between salicylate anions and positively charged Fe^{3+} centers. In this syntheses method, the capping agent, bridging agents, and solvents are chosen to not only control the shape, facets, and size of nanocrystals but also to ensure that the nanocrystals have a narrow distribution. At room temperature (298 K), iron nitrate is hydrolyzed in a basic medi (pH = 8) in the presence of salicylate, which acts as a capping agent The overall reaction is obtained by combining chemical equation (1) and (2). Thus, goethite nanocrystals are produced.

$$Fe(NO_3)_3 + 6\,H_2O = Fe(H_2O)_6(NO_3)_3 \quad (1)$$

$$Fe(H_2O)_6(NO_3)_3 + 3\,NaOH = \alpha\text{-}FeOOH + 3\,NaNO_3 + 7\,H_2O \quad (2)$$

$$2\,\alpha\text{-}FeOOH = \alpha\text{-}Fe_2O_3 + H_2O \quad (3)$$

When these nanoparticles are subjected to hydrothermal treatmen t at 348 K, goethite nanorods are obtained, which are enclosed by the following exposed facets: two {100}, two {110}, and two {001} . In this case, crystal growth takes place along {100}, {110}, and {001} surface, but maximum growth takes place along [001] direction. Th s means that salicylate moiety control the growth of (100) and (110) surfaces but growth is allowed on the z-direction due to wea interaction between (001) and salicylate. This is confirmed by obtained HRTEM images (Fig. 4). The formation of goet e nanorods is thermodynamically favored because it facilitates th growth of high energy surfaces. The surface energy of goethite crystal follows the following lattice order: γ{110} < γ{101} < γ{111}, < γ{001} < γ{100}, while the surface energy of these facets are 1.1 ,1.26, 1.33, 1.68, and 1.92 J m^{-2}, respectively.[58] By further increasing the hydrothermal temperature of these nanoparticles at 393 K, goethite nanoparticles are converted to hematite nanorods in the reaction represented by the chemical equation (3). The scheme 2 shows the crystal growth of these nanorods in [001] projec direction. In these nanorods, the following exposed facets: tw {001}, two {110}, two {120}, and two {210} are enclosed by 74.2% {001} + 25.8% {110}. However, maximum growth takes place alon the [300], [110] and its equivalent direction, while the maximum exposed surface is {001}. The {001} surface has the lowest energy o 1.66 J m^{-2}, so it is the most stable surface in these hematite nanorods. According to the theoretical density functional theor the calculated relaxed surface energy of hematite crystal follows the order: γ{001} < γ{012} < γ{110} < γ{100} < γ{101} < γ{111}, while e surface energy of these facets are 1.66, 1.92, 1.97, 2.19, 2.29, and 2.33 J m^{-2}, respectively.[59] When we further increased the synthesis temperature to 423 K, hematite nanocuboids were formed wit 100% exposed facet {012}. The scheme 2b shows the crystal growth of these nanocuboids in [2-21] project direction. At this temperature, only {012} facet and its equivalent surface grew to g exposed. Furthermore, at reaction duration of 36 hrs, we increased the synthesis temperature to 453 K and obtained nanocrystals o irregular shape. When the same temperature was maintained fo duration of 72 hrs, we obtained hematite nanocrystals, having th shape of bitruncated dodecahedron. In these nanocrystals, a greate number of high energy surfaces were exposed. Thus, the followin exposed facets: two {001}, twelve {104}, and six {100} were enclose with 27% {001} + 50.4% {104} + 22.6 % {100} facets. As shown i scheme 2c, the growth of the particle takes place along [001] an [100] direction, exposing the {104} surface to a maximum extent PXRD analysis showed that the relative intensity of (104) plane wa the highest. But, the (100) plane also had comparatively higher surface energy. By increasing the synthesis temperature to 473 K higher surface energy (101) planes are exposed

Scheme 2. Crystal structure of hematite having different indices and their growth direction project along: a) [001], b) [2-21], c) [010] and d) [010] direction.

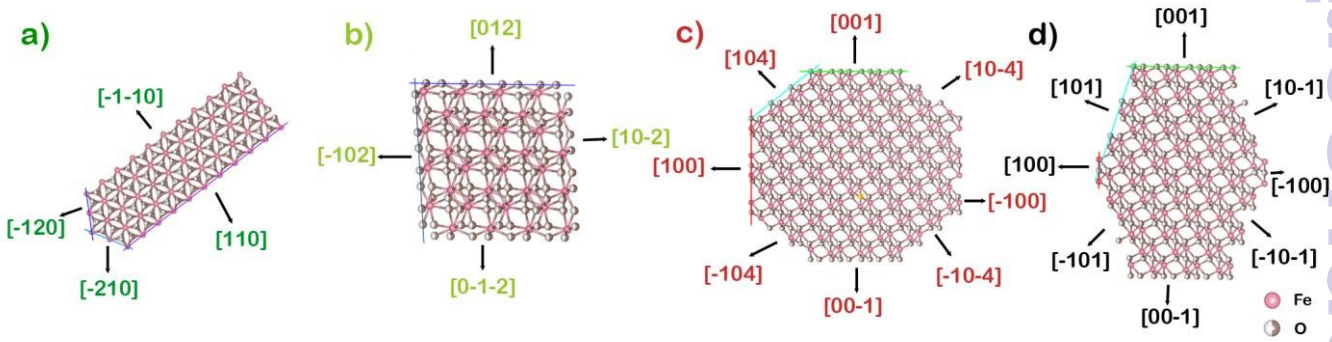

The Crystal structures of hematite explain the growth of a) nanorod b) nanocuboid c) truncated-dodecahedron and d) truncated-octahedron.

hematite nanocrystals growing along [001] and [100] direction (shown in scheme 2d). These nanocrystals have the shapes of bitruncated-elongated octahedron and bitruncated-octahedron (S200-BTEO and S200-BTO). Furthermore, these nanocrystals are enclosed by the highly exposed {101} surface. Thus, although all the primary parameters were kept fixed, the reaction temperature and duration were varied to control the morphology and exposed facets of nanocrystals. The analysis shows that planes of comparatively low surface energy get exposed when the synthesis temperature is low, whereas planes with higher surface energy get exposed when the synthesis temperature is high. Thus, temperature is the key parameter that controls the morphology of nanocrystals.

Photocatalysis

The photocatalytic reactivity of nanocatalyst is determined by its surface area, electronic, and atomic structure. BET N_2 sorption method is used to measure the surface area of hematite nanocrystals having different shapes.[60,61] As seen in Table 2, the surface area of all nanocrystals is almost similar, regardless of their shape. The electronic structures of hematite nanocrystals were determined by UV-Visible diffuse reflectance spectroscopy. Fig. 9a shows the absorption spectra of hematite nanocrystals. All the nanocrystals have shown absorption bands around 540–575 nm,[19] having band gap energies of 2.05, 1.99, 2.08, 2.01, and 2.06 eV for hematite nanorod (S120-NR), nanocuboid (S150-NC), bitruncated-dodecahedron (S180-BTD), bitruncated-elongated octahedron (S200-BTEO), and bitruncated-octahedron (S200-BTO), respectively. Fig. 9b shows the band gap energy profile of nanocrystals having the shape of bitruncated octahedron. Based on the analysis, we infer that the valence band and conduction band structures of these materials are identical. Moreover, the band gap energy of these nanocrystals lies in the visible region of the electromagnetic spectrum. We investigated the photocatalytic reactivity of hematite nanocrystals having different shapes by irradiating methyl orange (MO) with white light (λ>420 nm) in the presence of H_2O_2 (additive). Thus, methyl orange underwent degradation due to the photocatalytic reactivity of hematite crystals. The photocatalytic reaction was carried out using 0.02 mM methyl orange solution. Fig. 9c shows the decomposition rate of MO solution as a function. In Fig. 9c, C and C_0 represent the concentration of MO after and before irradiation. Fig. S5 shows the corresponding UV-Visible spectra obtained using nanocrystals of different shapes. As shown in Fig. S5a, MO solution underwent negligible photodegradation in the presence of light when catalysts and H_2O_2 were not added to the solution. In 180 min, only 12% of MO molecules underwent degradation. But, after the addition of hematite nanocrystals, the photodegradation rates increased rapidly. This indicates that hematite nanocrystals produced a highly reactive hydroxyl radical, promoting the photodegradation of MO in the presence of H_2O_2 and white light. In the photodegradation reaction, hydroxyl radicals catalyse the reduction of Fe^{3+} ions to Fe^{2+} ions through the photo Fenton reaction mechanism.[37]

$$\mathbf{Dye + photon \rightarrow Dye^*} \quad (4)$$

$$\mathbf{Fe^{3+} + Dye^* \rightarrow Fe^{2+} + Dye^{+\bullet}} \quad (5)$$

$$\mathbf{Fe^{2+} + H_2O_2 \rightarrow Fe^{3+} + {}^{\bullet}OH + OH^-} \quad (6)$$

$$\mathbf{Dye^{+\bullet}\ (or\ Dye) + {}^{\bullet}OH \rightarrow CO_2 + H_2O} \quad (7)$$

Following this mechanism of MO degradation over hematite nanocrystals, major degradation intermediates were identified by LC-MS and summarized in table S4 and confirmed by ESI-MS (Fig. S6 and S7). MO degradation takes place through N-demethylation and then destruction of azo bond. The proposed mechanism of MO degradation is shown in Fig. S8. A number of intermediate were identified by the liquid chromatography (retention time 1.79 min, m/z 304 denoted compound A; retention time 1.38 min, m/z 290 denoted compound B; retention time 1.06 min, m/z 97.1 denoted compound C). The performance of photocatalyst materials depend on so many parameter especially catalyst loading, the total optical power of light impinging on the sample and the substrate concentration.[62] From the Fig. 9C, we saw that hematite nanocrystals, having the shapes of nanorod, nanocuboid,

Table 2. Band gap energy and BET surface area of various hematite nanocrystals acting as photocatalysts in the degradation of MO; the photo-degradation rate and photocatalyst activity and apparent quantum efficiency (AQE).

Catalyst	Band gap (eV)	BET Surface Area (m^2g^{-1})	Rate ($\mu mol\ h^{-1}$)	Activity ($\mu mol\ h^{-1}g^{-1}$)	AQE ($x10^6$)
Nanorod	2.05	9.0	4.700	470.00	1.984
Nanocuboid	1.99	7.5	3.390	339.00	1.431
Bitruncated-dodecahedron	2.08	6.5	6.336	633.66	2.675
Bitruncated-elongated octahedron	2.01	7.0	a5.943	594.33	2.509
Bitruncated-octahedron	2.06	15.1	6.098	609.84	2.574

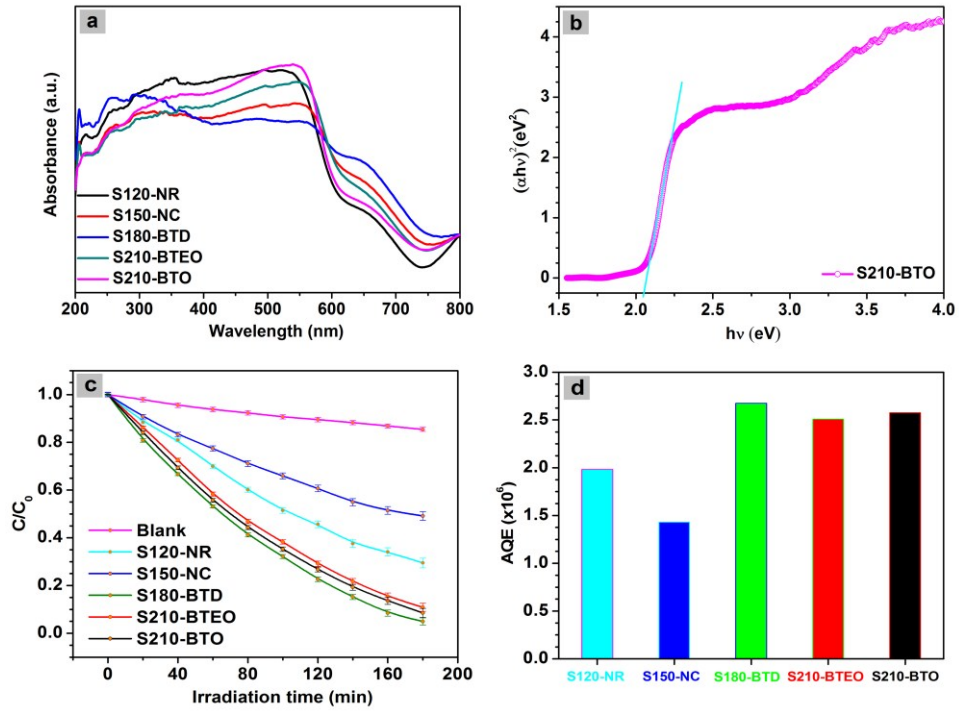

Fig. 9. a) UV–visible diffused reflectance spectra of hematite nanocrystals with indexing sample name. b) The band gap energy of nanocrystals, having the shape of bitruncated-octahedron (S200-BTO). c) The photodegradation rate of MO dye using various types of hematite nanocrystals as photocatalyst. Reaction conditions: 50 ml MO of concentration 0.02 mM, catalyst 10 mg, 0.5 mL of H_2O_2 (30 % w/) solution, initial pH 6.2, solar simulator with 150 W Xenon-lamp (cut-off filter 420 nm) with an average light intensity of 92.33 mWcm^{-2}. d) The apparent quantum efficiency of corresponding S120-NR, S150-NC, S180-BTD, S200-BTEO, and S200-BTO shaped photocatalyst.

bitruncated-dodecahedron, bitruncated-elongated octahedron, and bitruncated-octahedron, show 70.2, 51.8, 96.5, 89.2 and 91.4 % MO degradation efficiency, respectively. For comparing the photocatalytic activity of these shaped materials, the apparent quantum efficiency (AQY)[62-64] was calculated using the following formula given below:

$$\varphi_{(MO)} = \frac{\mp d[MO]/dt}{d[hv]_{inc}/dt}$$

Where d[MO]/dt is the rate of change of the concentration of the MO and $d[hv]_{inc}/dt$ is the total optical power impinging on the sample. Here AQE does not take in to account the fraction of light absorbed by hematite photocatalyst. The rate of change of MO was measured from reaction mixture. The white light (λ>420 nm) was illuminated in the 45.2 cm^2 reaction area with 92.33 mWcm^{-2} light intensity and $4.027x10^{17}$ cm^{-2}s^{-1} photon flux. The measured AQE are listed in table 2 and plotted in Fig. 9d for nanorod, nanocuboid, bitruncated-dodecahedron, bitruncated-elongated octahedron, and bitruncated-octahedron, and these shaped nanocrystals show different degradation efficiency, and AQE were 1.984 x 10^{-6}, 1.431 x 10^{-6}, 2.675 x 10^{-6}, 2.509 x 10^{-6}, 2.574 x 10^{-6} respectively. As nanocrystals of different shapes have different exposed facets, they show different catalytic activity. Table 1 displays the exposed percentages of nanocrystals having different shapes and exposed facets. In this table, the exposed surfaces nanorods have

%{001} + 25.8 % {110}, nanocuboid have 100 % {012}, bitruncated-dodecahedron have 27 % {001} + 50.4 % {104} + 22.6 % {100}, bitruncated-elongated octahedron have 3.5 % {001} + 96.5 % {101} and bitruncated-octahedronhave 5.2 % {001} + 94.8 % {101} exposed surfaces. The atomic arrangements of these surfaces are different in nanocrystals of different shapes. While catalyzing the degradation of MO dye, the exposed Fe^{3+} is the main active centre. Sun and coworkers[31] have reported that different atomic planes have different Fe^{3+} density due to their atomic arrangements. The density of exposed Fe^{3+} on (012), (001), (110), (104), and (100) planes was 0.0733, 0.0911, 0.100, 0.103, and 0.1158 [$Å^{-2}$], respectively. So, with a high density of 50.4 % {104} + 22.6 % {100} planes, hematite nanocrystals having the shape of a bitruncated-dodecahedron showed maximum photocatalytic activity. In contrast, with a low density of 100 % {012}, nanocuboid nanocrsytals had lowest photocatalytic activity among all the nanocrystals. Thus, the photocatalytic activity of different nanocrystals was in the following order: {104}+{100}+{001} (bitruncated-dodecahedron) >{101}+{001} (bitruncated-octahedron) >{001}+{110} (nanorods) >{012} (nanocuboid). In the photocatalytic reaction, after the completion of the reaction, the catalyst was recovered by an external magnet (Fig. S9) and was washed thoroughly with water and ethanol. We also examined the reusability of hematite nanocrystals. According to the results shown in Fig. S10, the catalyst has very high recycling efficiency as it could be used in six consecutive cycles.

CONCLUSION

In conclusion, we have developed a very simple and environmentally friendly method of synthesizing goethite and hematite nanocrystals having different shapes. The temperature controls the growth and shape of nanocrystals. Nanocrystals of different morphologies could be obtained by tuning the reaction temperature, while the growth of nanocrystals was related to the surface energy of the growing plane. Depending on the surface energy and temperature of the reaction, nanocrystals of different shapes exposed the following different facets: {001}, {110}, {100}, {012}, {104} and {101}. The synthesis process shows that we can control the size, shape, and facets of the nanocrystals simply by tuning the reaction temperature. The size of nanocrystals increases when the hydrothermal temperature and duration of the reaction are increased. At higher temperatures, we could obtain complex polyhedron nanocrystals. All the three dimensions of these complex nanocrystals were stable as per Euler's Formula. Hematite nanocrystals showed high photocatalytic activity that stimulated MO degradation in the presence of white light. The nanocrystals with bitruncated-dodecahedron shape had high Fe^{3+} density in surface {100} + {104}. So, these nanocrystals were found to have highest catalytic activity among all hematite nanocrystals. Nanocuboid nanocrystals had the lowest catalytic activity with low Fe^{3+} density in surface {012}. In addition to the removal of pollutants, these newly synthesized hematite nanocrystal can find possible applications in hydrogen generation through water splitting and Li ion battery.

Acknowledgements

SKK hanks the senior research fellows working at Council of Scientific and Industrial Research (CSIR), New Delhi. AB wishes to thank Department of Science and Technology (DST), New Delhi for providing instrumental facility through Nano Mission Initiative, DST-SERB, DST-UKIERI project grants. DK received grant by the National Research Foundation of Korea, which is funded by the Korea Government (MEST) (NRF-2009-0093033, NRF-2010-0027955 and NRF-2012R1A2A1A05026313).

Notes and references

1. C. T.Campbell and J. Sauer, *Chem. Rev*., 2013, **113**, 3859-3862.
2. N. Tian, Z.-Y. Zhou, S.-G. Sun, Y. Ding and Z. L.Wang,. *Science* 2007, **316**, 732-735.
3. A. Erlebach, H.-D. Kurland, J. Grabow, F. A. Müller and M. Sierka *Nanoscale*, 2015, **7**, 2960–2969.
4. Z.-Y. Zhou, N. Tian, J.-T. Li, I. Broadwell and S.-G. Sun, *Chem. Soc. Rev*., 2011, **40**, 4167-4185.
5. J. F. Weaver, *Chem. Rev*., 2013, **113**, 4164-4215.
6. C. I. Cheng, Y.-P. Chang and Y.-H. Chu, *Chem. Soc. Rev*., 2012, **41**, 1947-1971.
7. X. Lang, W. Hao, W. R. Leow, S. Li, J. Z. and X. Chen, *Chem. Sci*. 2015, **6**, 5000–5005**.**
8. Q. Kuang, X. Wang, Z. Jiang, Z. Xie and L. Zheng, *Acc. Chem. Res*. 2014, **47**, 308-318.
9. L. Manna, D. J. Milliron, A. Meisel, E. C. Scher and A. P. Alivisatos, *Nat. Mater,* 2003, **2**, 382-385.
10. J. Gong, *Chem. Rev*., 2012, **112**, 2987-3054.
11. E. C. Dreaden, A. M. Alkilany, X. Huang, C. J. Murphy and M. A. El-Sayed, *Chem. Soc. Rev*., 2012, **41**, 2740–2779.
12. M. H. Huang and C.-Y. Chiu, *J. Mater. Chem. A*, 2013, **1**, 8081 - 8092.
13. Z. Quan, Y. Wang and J. Fang, *Acc. Chem. Res*., 2013, **46**, 191 - 202.
14. M. H. Huang, S. Rej and S.-C. Hsu, *Chem. Commun*., 2014, **50**, 1634—1644.
15. W. Zang, G. Li, L. Wangab and X. Zhang, *Catal. Sci. Technol*., 2015, **5**, 2532–2553.
16. S. Rej, H.-J. Wang, M.-X. Huang, S.-C. Hsu, C.-S. Tan, F.-C. Lin, J.-S. Huang and M. H. Huang, *Nanoscale*, 2015, **7**, 11135–11141
17. L. Polavarapu, S. Mourdikoudis, I. Pastoriza-Santos and J. Pérez-Juste, *CrystEngComm*, 2015, **17**, 3727–3762.
18. A. K. Patra, A. Dutta, and A. Bhaumik, *J. Phys. Chem. C,* 2014, **118**, 16703−16709.
19. A. K. Patra, A. Dutta and A. Bhaumik, *ACS Appl. Mater. Interfaces,* 2012, **4**, 5022-5028.
20. X. Mou, X. Wei, Y. Li and W. Shen, *CrystEngComm*, 2012, **14**, 5107–5120.
21. L. B. Wang, L. X. Song, Z. Dang, J. Chen, J. Yang and J. Zeng, *CrystEngComm*, 2012, **14**, 3355–3358.
22. M. Cao, T. Liu, S. Gao, G. Sun, X. Wu, C. Hu and Z. L. Wang, *Angew. Chem. Int. Ed*., 2005, **44**, 4197 –4201.
23. Z.-H. Ruan, J.-H. Wu, J.-F. Huang, Z.-T. Lin, Y.-F. Li, Y.-L. Liu, P.-Y. Cao, Y.-P. Fang, J. Xie and G.-B. Jiang, *J. Mater. Chem. A*, 2015, **3**, 4595–4603.

24. L. Sun, X. Han, K. Liu, S. Yin, Q. Chen, Q. Kuang, X. Han, Z. Xie and C. Wang, *Nanoscale*, 2015,**7**, 9416-9420.
25. M. Mahmoudi, A. S. Milani and P. Stroeve, *Int. J. Biomed. Nanosci. Nanotechnol*. 2010, **1**, 164-201.
26. F. Zheng, M.He, Y. Yang and Q. Chen, *Nanoscale*, 2015, **7**, 3410–3417.
27. J. S. Cho, Y. J. Hong, J.-H. Lee and Y. C. Kang, *Nanoscale*, 2015, **7**, 8361–8367.
28. X. Qi, G. She, X. Huang, T. Zhang, H. Wang, L. Mu and W. Shi, *Nanoscale*, 2014, **6**, 3182–3189.
29. M. Wang, M. Pyeon, Y. Gönüllü, A. Kaouk, S. Shen, L. Guo and S. Mathur, *Nanoscale*, 2015, **7**, 10094–10100.
30. D. A. Wheeler, G. Wang, Y. Ling, Y. Li and J. Z. Zhang, *Energy Environ. Sci*., 2012**, 5**, 6682–6702.
31. X. Mou, X. Wei, Y. Li and W. Shen, *CrystEngComm*, 2012, **14**, 5107–5120.
32. S. Xie, H. Jia, F. Lu, N. Sun, J. Yu, S. Liu and L. Zheng, *CrystEngComm*, 2015, **17**, 1210–1218.
33. J. Yin, Z. Yu, F. Gao, J. Wang, H. Pang and Q. Lu, *Angew. Chem. Int. Ed*., 2010, **49**, 6328-6332.
34. X. Wang, J. Wang, Z. Cui, S. Wang and M. Cao, *RSC Adv*., 2014, **4**, 34387-34394.
35. L. Chen, X. Yang, J. Chen, J. Liu, H. Wu, H. Zhan, C. Liang, and M. Wu, *Inorg. Chem*. 2010, **49**, 8411–8420.
36. B. Lv, Z. Liu, H. Tian, Y. Xu, D. Wu and Y. Sun, *Adv. Funct. Mater.,* 2010, **20**, 3987-3996.
37. R. Liu, Y. Jiang, H. Fan, Q. Lu, W. Du and F. Gao, *Chem. Eur. J*., 2012, **18**, 8957-8963.
38. X. Zhou, J. Lan, G. Liu, K. Deng, Y. Yang, G. Nie, J. Yu and L. Zhi, *Angew. Chem. Int. Ed*., 2012, **51**, 178-182.
39. Y. Zhao, F. Pan, H. Li, T. Niu, G. Xu and W. Chen, *J. Mater. Chem. A,* 2013, **1**, 7242-7246.
40. J. Ouyang, J. Pei, Q. Kuang, Z. Xie and L. Zheng, *ACS Appl. Mater. Interfaces*, 2014, **6**, 12505-12514.
41. M. Lin, L. Tng, T. Lim, M. Choo, J. Zhang, H. Tan and S. Bai, *J. Phys. Chem. C*, 2014, **118**, 10903−10910.
42. L. Leon-Reina, J. M. Compana, Á. G. De la Torre, R. Moreno, L. E. Ochando and M. A. G. Aranda, *Powder Diffraction,* 2011, **26**, 48-52.
43. B. Wang, H. Wu, L. Yu, R. Xu, T.-T. Lim and X. W. Lou, *Adv. Mater*., 2012, **24**, 1111-1116.
44. A. K. Patra, A. Dutta, A. Bhaumik, *Chem. Eur. J*., 2013, **19**, 12388-12395.
45. L. Wang and L. Gao, *J. Phys. Chem. C*, 2009, **113**, 15914-15920.
46. P. Basnet, G. K. Larsen, R. P. Jadeja, Y.-C. Hung and Y. Zhao, *ACS Appl. Mater. Interfaces*, 2013, **5**, 2085-2095.
47. D. L. A. de Faria, S. Venâncio Silva and M. T. de Oliveira, *J. Raman Spectrosc*., 1997, **28**, 873-878.
48. K. F. McCarty, *Solid State Commun*., 1988, **68**, 799-802.
49. H. Cao, X. Qian, C. Wang, X. Ma, J. Yin and Z. Zhu, *J. Am. Chem. Soc*., 2005, **127**, 16024-16025.
50. P. Ou, G. Xu, Z. Ren, X. Hou and G. Han, *Mater. Lett.,* 2008, **62**, 914-917.
51. J. Kang, Q. Kuang, Z.-X. Xie and L.-S. Zheng, *J. Phys. Chem. C*, 2011, **115**, 7874-7879.
52. S. He, G.-S. Wang, J.-W. Wang, Y.-Z. Wei, Y. Wu, L. Guo and M.-S. Cao, *ChemPlusChem,* 2013, **78**, 875-883.
53. X. Li, W.Wei, S. Wang, L. Kuai and B. Geng, *Nanoscale*, 2011, **3**, 718–724.
54. P. Cubillas and M. W.Anderson, Synthesis Mechanism: Crystal Growth and Nucleation. In Zeolites and Catalysis, Wiley-VCH Verlag GmbH & Co. KGaA: 2010. pp 1-55.
55. A. K. Patra, S. K. Kundu, D. Kim and A. Bhaumik, *ChemCatChem*, 2015, **7**, 791-798.
56. V. Kumari, A. K. Patra and A. Bhaumik, *RSC Adv*., 2014, **4**, 13626-13634.
57. A. K. Patra, A. Dutta A. Bhaumik, *J. Hazard. Mater*., 2012, **201–202**, 170-177.
58. N. H. de Leeuw and T. G. Cooper, *Geochim. Cosmochim. Acta*, 2007, **71**, 1655-1673.
59. N. Dzade, A. Roldan and N. A de Leeuw, *Minerals,* 2014, **4**, 89-115.
60. A. K. Patra, A. Dutta and A. Bhaumik, J. *Solid State Chem*., 2014, **215**, 135-142.
61. N. Pal, E.-B. Cho, D. Kim and M. Jaroniec, *J. Phys. Chem. C*, 2014, **118**, 15892-15901.
62. J. M. Buriak, P. V. Kamat and K. S. Schanze, *ACS Appl. Mater. Interfaces,* 2014, **6**, 11815−11816.
63. M. R. Hoffmann, S. T. Martin, W.Choi and D. W. Bahnemannt, *Chem. Rev*. 1995, **95**, 69-96.
64. K. Lee, D. A. Ruddy, G. Dukovic and N. R. Neale, *J. Mater. Chem. A*, 2015, **3**, 8115–8122.

